nature nanotechnology

ARTICLES

https://doi.org/10.1038/s41565-021-00878-4

Bioelectronic control of a microbial community using surface-assembled electrogenetic cells to route signals

Jessica L. Terrell[1,7], Tanya Tschirhart[2,7], Justin P. Jahnke[1], Kristina Stephens[3,4,5], Yi Liu[3,5], Hong Dong[1], Margaret M. Hurley[6], Maria Pozo[3], Ryan McKay[3,4,5], Chen Yu Tsao[3,4,5], Hsuan-Chen Wu[3,5], Gary Vora[2], Gregory F. Payne[3,4,5], Dimitra N. Stratis-Cullum[1] and William E. Bentley[3,4,5] ✉

We developed a bioelectronic communication system that is enabled by a redox signal transduction modality to exchange information between a living cell-embedded bioelectronics interface and an engineered microbial network. A naturally communicating three-member microbial network is 'plugged into' an external electronic system that interrogates and controls biological function in real time. First, electrode-generated redox molecules are programmed to activate gene expression in an engineered population of electrode-attached bacterial cells, effectively creating a living transducer electrode. These cells interpret and translate electronic signals and then transmit this information biologically by producing quorum sensing molecules that are, in turn, interpreted by a planktonic coculture. The propagated molecular communication drives expression and secretion of a therapeutic peptide from one strain and simultaneously enables direct electronic feedback from the second strain, thus enabling real-time electronic verification of biological signal propagation. Overall, we show how this multifunctional bioelectronic platform, termed a BioLAN, reliably facilitates on-demand bioelectronic communication and concurrently performs programmed tasks.

Communication, the sending and receiving of information, drives coordinated function across a variety of systems and at many scales. Most distinct are natural biological processes and electronic technologies, with notably dissimilar communication modalities. Biological information is often transmitted as diffusion gradients of ions and small molecules. By contrast, electronic systems require electron flow, and are often wirelessly networked to extend digital communication and capabilities beyond single devices[1]. It follows that if a robust hybrid communication modality were developed, biological and electronic systems could be similarly networked in next-generation bioelectronics platforms[2]. We suggest that a redox modality can serve as this bridge.

There are several means to link electronics with biology, for example though direct electron transfer[3,4], optical signalling (for example optogenetics)[5,6] and potential-mediated ion flows[7]. Recently, redox-active molecules were introduced as another bioelectronic signalling medium[8–10]. Redox-active molecules are well suited for bioelectronic communication by serving dually as electron carriers and biomolecular species, where electron flow is coupled to interconversion between biologically distinct redox states[11]. Routine electrochemical instrumentation provides a programmable electronic interface, where redox events are directed in real time by voltage parameters and use minimal infrastructure for versatile, miniaturizable and in situ implementation[12]. This provides an expedient tool to electronically access a wide repertoire of biomolecules and redox-sensitive proteins, thus potentially controlling biorecognition and associated genetic machinery[13,14].

Tschirhart et al. have previously realized the concept of 'electrogenetics', where electronic input was relayed using a redox mediator to dynamically activate gene expression in *Escherichia coli*[8,15]. In the present work, electrode-generated redox signals, without mediators and with surface-engineered bacteria, initiate transduction and, when coupled with a second, recognition-based redox event, propagate and validate information flow between the electronic system and a community of engineered microbial cells such that an electronically controlled biological local area network (BioLAN, Fig. 1a) is created. We use the principles of synthetic biology to coopt native redox signalling for modular circuitry that coordinates information processing across populations.

The electrochemically plugged-in BioLAN serves as an embedded, biological local area network that transmits electronic information. The BioLAN's community nature provides several advantages—signal propagation, spatial organization and division of labour across populations[16,17]. Each member is engineered for specific signal processing tasks—signal routing, verification and bio-actuation (Fig. 1). Initially, electronic input is redox-gated for electronic-to-bio signal transduction. The electrochemical reduction of molecular oxygen to hydrogen peroxide (henceforth, 'peroxide') is paired with a peroxide-inducible genetic circuit derived from the OxyR oxidative stress response regulon[18]. Once repurposed as an electrogenetic gate, cells are able to translate redox input into an orthogonal molecular cue (acyl homoserine lactone (AHL) from *Pseudomonas aeruginosa*) for information routing (Fig. 1b).

[1]U.S. Army Combat Capabilities Development Command (DEVCOM)—Army Research Laboratory, Adelphi, MD, USA. [2]Center for Biomolecular Science and Engineering, U.S. Naval Research Laboratory, Washington, DC, USA. [3]Fischell Department of Bioengineering, University of Maryland, College Park, MD, USA. [4]Fischell Institute for Biomedical Devices, University of Maryland, College Park, MD, USA. [5]Institute for Bioscience and Biotechnology Research, University of Maryland, College Park, MD, USA. [6]U.S. Army Combat Capabilities Development Command (DEVCOM)—Army Research Laboratory, Aberdeen, MD, USA. [7]These authors contributed equally: Jessica L. Terrell, Tanya Tschirhart. ✉e-mail: bentley@umd.edu

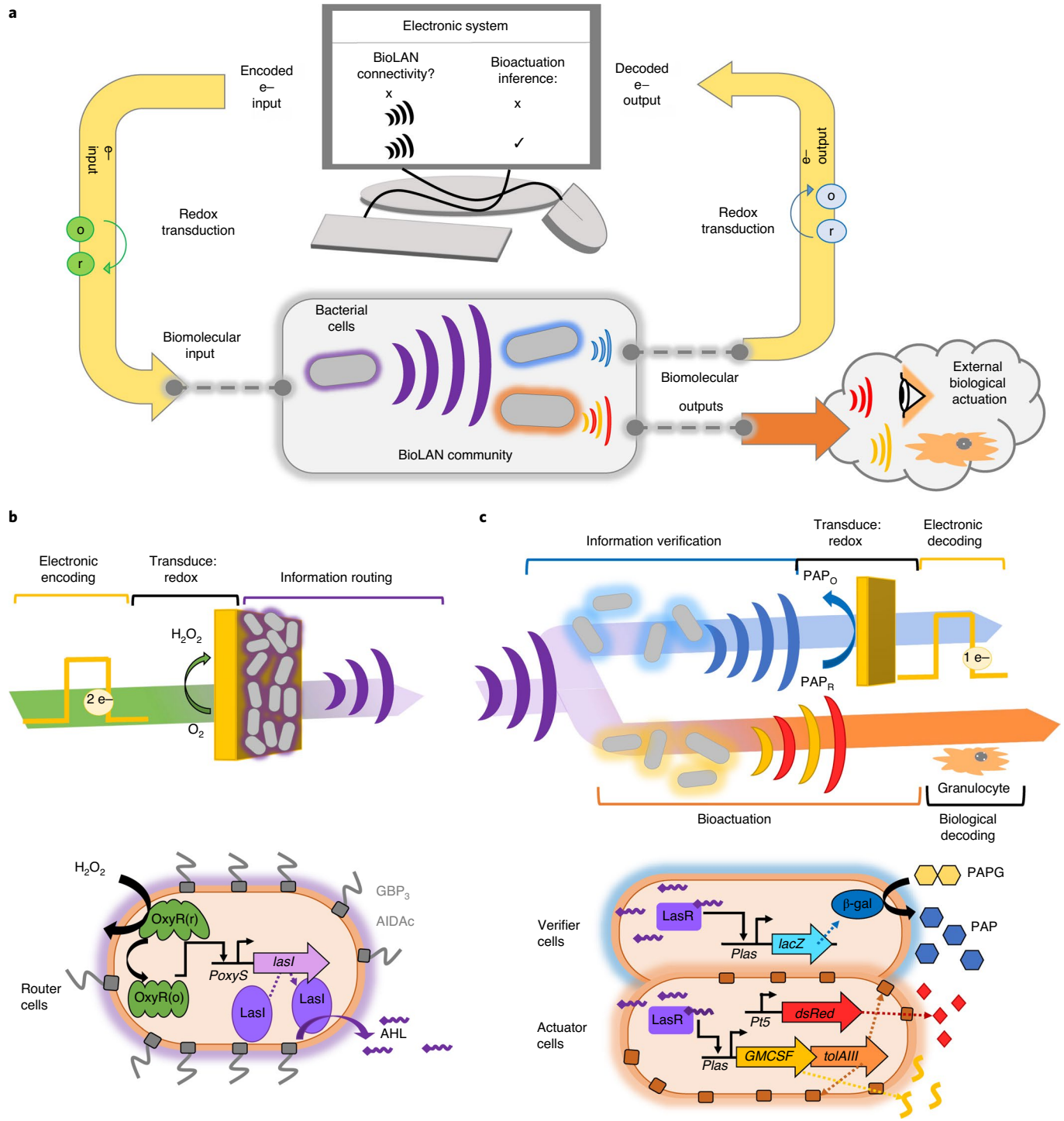

Fig. 1 | Information flow through an electronically interfaced biological network. a, Connectivity between electronics and a microbial community is established using biomolecular redox events to transduce bioelectronic signalling by simultaneously mediating electron flow and eliciting biological interactions. The result is an electronically controlled BioLAN that propagates the signal across microbial subpopulations and on to external environments for multiplexed actuation. One subpopulation transduces received information into an electronic output that returns BioLAN system status and a second produces biological outputs. o, oxidized; r, reduced. **b**, Electronic-encoded input is transduced to a biologically recognized signal, hydrogen peroxide, via electrochemically controlled oxygen reduction. BioLAN cells assembled at the electrode (via a gold-binding peptide surface display, GBP_3–AIDAc) intercept peroxide to activate electrogenetic expression of LasI. LasI then synthesizes AHL for signal routing. **c**, Through AHL activation, the BioLAN indirectly connects additional cells to electrogenetically controlled events. Verifier cells detect the routed AHL signal via LasR and produce the β-gal enzyme. β-gal cleaves PAPG to PAP, which is detected by electrochemical oxidation. This acts to transmit the propagated signal back to the electronics and thereby reports on BioLAN system connectivity. Additionally, actuator cells respond identically to the AHL signal by upregulating TolAIII-mediated membrane porosity, which co-releases a therapeutically relevant GMCSF and overexpresses DsRedExpress II fluorescent protein out of the cell via diffusion. PAP_O, oxidized PAP; PAP_R, reduced PAP.

Importantly, these routing cells are 'hardwired' to the active electrode via engineered surface adhesion. This enables direct, uniform interception of the peroxide signal and its transmission as AHL to the remaining BioLAN constituents.

The BioLAN includes two mobile populations of AHL recipients that interpret and relay signals downstream; thus a signal pathway from 'encoded' electronic input to multiplexed genetic activation is established via AHL (Fig. 1c). Verifier cells confirm the relayed information, providing an electronically measured response through expression of β-galactosidase (β-gal) and its cleavage of 4-aminophenyl-β-D-galactopyranoside (PAPG) to the electronically detected *p*-aminophenol (PAP)[19,20]. Bioactuator cells are also induced by AHL, directing the synthesis and secretion of a hard-to-detect therapeutic, granulocyte macrophage colony-stimulating factor (GMCSF)[21]. Importantly, the electronic output from verifier cells serves to indicate (1) successful signal propagation and information transfer into the BioLAN, and, because their signal-receiving genetic circuitry is identical to that of the actuator cells, (2) the synthesis of GMCSF. Thus, BioLAN signalling both commands and confirms putative delivery of the therapeutic. That is, bidirectional (electronic-to-bio-to-electronic) communication across a bioelectronics interface can be established by taking advantage of the redox-specific biological processing of electrochemically encoded and decoded information. The resulting bioelectronics platform, including an electronically plugged-in microbial BioLAN, fulfils the fundamental requirements for implementing remote biological functions within networked biohybrid devices.

OxyR-based electrogenetics for bioelectronic signal transduction

To encode and transduce electronic information for cells, we developed an electrogenetic system using the native transcriptional activator OxyR. *E. coli* rapidly takes up and enzymatically degrades peroxide upon exposure, and its transient intracellular presence oxidizes OxyR (OxyR(o))[22,23]. This can elicit a strong native regulatory response, including upregulation of *oxyS* from the *PoxyS* promoter[24,25]. For electrogenetic system development, peroxide can be electrochemically generated from oxygen under physiological conditions[26].

For peroxide-driven gene induction, we harnessed an OxyR-regulated genetic circuit paired with constitutive OxyR expression[27] for peroxide-induced expression of genes of interest (*sfGFP*, *lacZ* and *lasI*) from the *PoxyS* promoter (Fig. 2a). We found that *E. coli* tolerated up to 100 μM peroxide with negligible effect on cell viability. At these levels, near-saturated OxyR(o) levels were predicted and gene expression was characterized as a function of peroxide dose and time (see kinetic models, Supplementary Figs. 1–3). Thus, in agreement with previous reports, 0–100 μM peroxide provided a benign induction range[28]. Further, we found that OxyR was mostly oxidized (peak $f_{\mathrm{OxyR(o)}} \sim 0.6$, Fig. 2b), leading to near-saturated expression levels. In analogous timecourse experiments with 25 μM peroxide, LasI-generated AHL levels and β-gal peaked 60 min after induction (Fig. 2c), also in agreement with modelled kinetics. Overall, the consistency of modelled behaviour with experimental data validated the OxyR kinetic predictions. This, along with induction dependence on cell number and protein degradation (Supplementary Fig. 4), provided design insights for further electrogenetic studies.

We next induced OxyR-regulated gene expression via electronic input in lieu of exogenously added peroxide. Peroxide can be electrochemically generated at physiological conditions (pH 7) and benign voltages (approximately −0.3 to −0.9 V versus Ag/AgCl)[26] by the partial reduction of oxygen, according to

$$O_2 + 2H^+ + 2e^- \leftrightarrow H_2O_2 \quad (1)$$

Peroxide thus provides a transduction mechanism by which electronic input can be converted into a biologically recognized cue in our system (Fig. 2d). Previous electrogenetics work coopted the SoxRS regulon, requiring purposely added redox mediators to facilitate electron exchange between the electrode and nearby cells[8,18]. Here, no supplemental redox mediators are needed. For design studies, we biased an electrode at −0.4 V to reduce oxygen in amounts stoichiometrically proportional to applied charge. External influences on charge transfer impact the rate of peroxide generation, including electrode dimensions (Fig. 2e), media and oxygen availability. Regardless, we found that the energy efficiency of oxygen reduction to peroxide was near constant (59%, Supplementary Fig. 5). Applied charge, then, reliably represents a unit of 'electroinduction dose' and, conveniently, has electrode-area-based proportionality.

We then tested electrogenetic induction by monitoring the β-gal activity of suspended cells using a 50 mm^2 surface. In Fig. 2f, activity increases over time and as a function of charge (current × time). All electroinduced samples exhibited activity above basal levels within 5 min. With a maximum dose, expression levels were on par with a 25 μM exogenously induced control, which is indicative of having reached expression-saturating OxyR(o) levels. We saw similar charge-based induction of sfGFP and verified that growth behaviour did not differ between electrochemically produced and exogenously supplied peroxide conditions (Supplementary Fig. 6). Thus, this novel electrogenetic circuit enables us to link direct electronic input, through redox transduction, to biological behaviour.

Elucidation of the bioelectronic interface

Electrode-generated peroxide in a quiescent fluid creates a far more conducive signalling environment compared with its exogenous addition to a planktonic culture, where peroxide must be uniformly mixed. We studied the spatiotemporal dynamics of each process to elucidate optimal conditions for uniform electrogenetic induction.

First, we simulated the peroxide gradient at the electrode in the presence of unstirred planktonic cells on the basis of its generation rate, diffusion and cellular consumption (Supplementary Methods). The model data in Fig. 3a show that peroxide reaches micromolar concentrations proximal to an electrode surface within seconds of a voltage bias. Despite substantial peroxide consumption by cells (Supplementary Fig. 1), their presence as a planktonic population only marginally attenuates the bulk concentration (Supplementary Fig. 7). Conversely, in a scenario where the entire cell population is distributed at the electrode surface, nearly all generated peroxide is intercepted, limiting its accumulation in bulk to 1.5 μM at its peak (Fig. 3b). Once peroxide generation ceases, the simulation shows an interfacial zone of complete elimination by the bacterial monolayer within 1 min.

We next analysed the effect of cell position on OxyR dynamics. In Fig. 3c,d, we found that the cells' consumption near the electrode greatly limits the peroxide quantity available for distal cells, whereas all electrode-localized cells provide uniform consumption. For planktonic populations in the simulation, fewer than 7% of the cells experience maximal OxyR activation in a peroxide-rich environment (that is at least 25 μM peroxide, whereby $f_{\mathrm{OxyR(o)}} \geq 0.6$) near the electrode surface (denoted Z1). The peroxide concentration declines with distance, resulting in the majority of cells (82%) positioned furthest from the electrode (Z3) experiencing minimal peroxide levels (<4 μM) and hence minimal OxyR activation ($f_{\mathrm{OxyR(o)}} \leq 0.1$). By contrast, the fractions of activated OxyR and, consequently, of induced cells are higher for electrode-localized cells—achieving $f_{\mathrm{OxyR(o)}} = 0.9$ universally within 5 min of voltage bias (Fig. 3d).

Additionally, we note that these electroinduction parameters (that is immobilized configuration of the bioelectronics interface, 300 s voltage duration) yield net peroxide uptake nearly equivalent to 25 μM induction (Supplementary Fig. 8), which was shown to sufficiently saturate protein expression (Fig. 2b). Thus, these

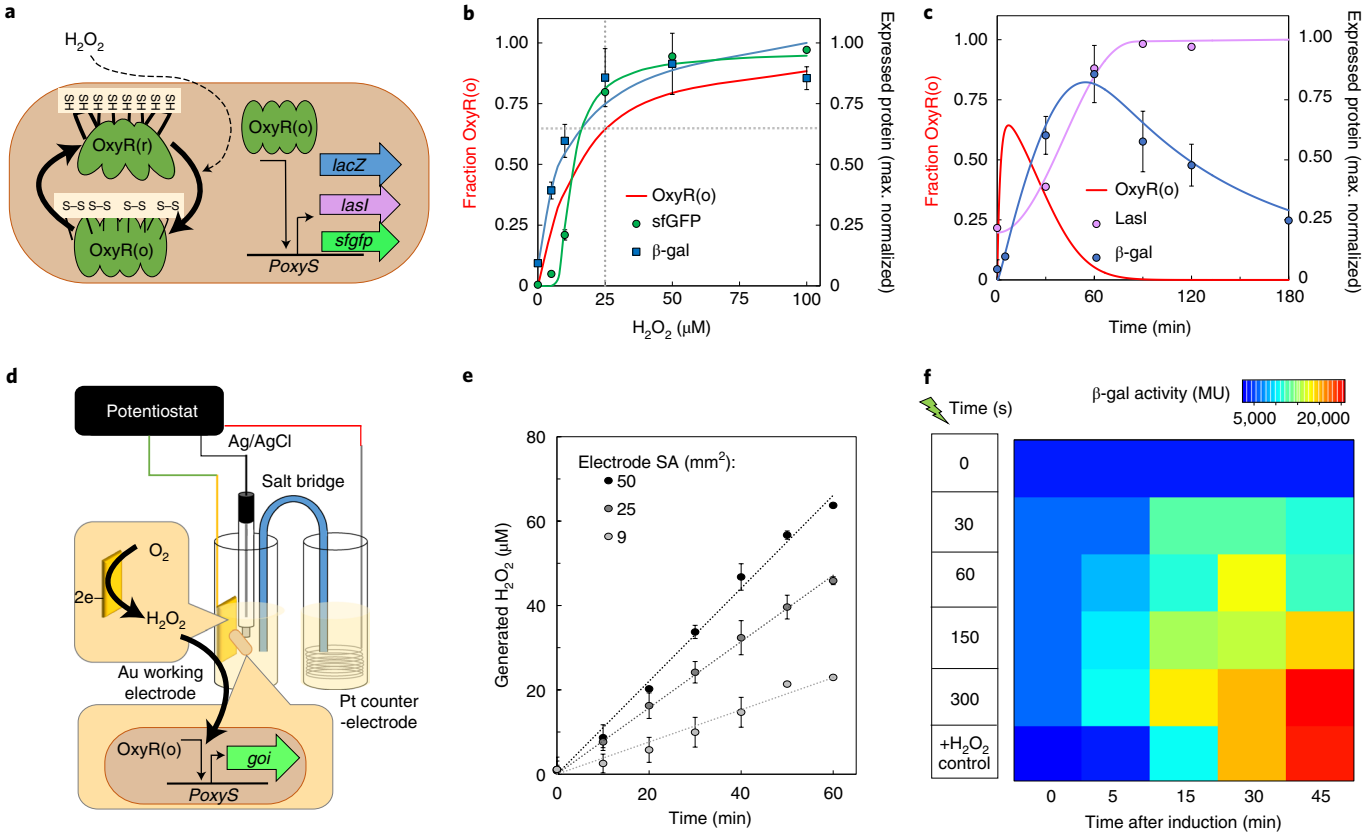

Fig. 2 | Peroxide-driven electrogenetic control. a, OxyR-regulated gene expression: hydrogen peroxide oxidizes OxyR, resulting in disulfide bond formation. OxyR(o) activates expression of a gene of interest (goi) under the *PoxyS* promoter. **b**, Dose–response of model-predicted intracellular OxyR(o) fraction at 10 min (Supplementary Fig. 1) and saturation-normalized expression of reporter proteins (β-gal, sfGFP) to hydrogen peroxide, measured by Miller assay (at 60 min) and flow cytometry (at 45 min), respectively. Experimental data are indicated by data points. Fitted models of relative protein levels are shown as solid lines. Dotted lines indicate the induction threshold (25 μM peroxide) and corresponding OxyR(o) peak ($f_{OxyR(o)} = 0.644$) required to achieve saturated protein expression. **c**, Timecourse of model-predicted intracellular OxyR(o) fraction and data of saturation-normalized expression levels of reporter proteins (β-gal, LasI (indicated by AHL level), each ssrA tagged) when induced by 25 μM peroxide. Experimental data are indicated by data points and fitted models of protein levels are shown as solid lines. **d**, Schematic of set-up for electrochemical reduction of oxygen to hydrogen peroxide to drive OxyR(o)-mediated gene expression. **e**, Measured peroxide concentration in the working electrode solution over time, with a constant −0.4 V applied to electrodes of indicated surface areas (SA). Data in **b**,**c** represent means of biological triplicates and data in **e** represent means of technical triplicates. Error bars represent s.d. **f**, Electrogenetic β-gal expression, assayed over 45 min in response to the indicated electrochemical pulse lengths at −0.4 V using a 50 mm² electrode. The '0' condition indicates basal β-gal activity. For the '+H_2O_2' positive control, 25 μM hydrogen peroxide was exogenously added. MU, Miller units.

design studies for in situ peroxide generation elucidate favourable conditions that should enable strong gene expression (for example for LasI-mediated AHL signalling) and, overall, provide a fast, efficient and uniform bioelectronic information-transfer interface.

Electrode immobilization of electrogenetic cells

To localize signal transfer at the bioelectronic interface, cells were engineered to enable direct assembly onto the electrode via peptide-mediated affinity interactions. We harnessed the outer membrane autotransporter pore-forming protein (AIDAc) as a vector for cell surface modification[29,30]. We fused AIDAc with a recombinant peptide consisting of a trimeric repeat of a non-natural peptide characterized for its high affinity to gold (GBP_3)[31–33]. Our structural prediction of the GBP_3–AIDAc fusion (Fig. 4a) depicts the peptide's extrusion through the centre of the AIDAc barrel as a relatively unstructured, extended conformation.

Surface-displayed expression of GBP_3 was initially tested by quantum dot labelling, which showed affinity for the GBP_3^+ and not the GBP_3^- cell surface, presumably due to the Zn-containing quantum dot shell and the peptide's histidine tag through well known affinity interactions with transition metals (Supplementary Fig. 9)[34]. Furthermore, by transmission electron microscopy, gold nanoparticles did not associate with cells lacking GBP_3 (Fig. 4b), but showed retention on GBP_3^+ cell surfaces (Fig. 4c). We found that GBP_3^+ cells bound with 50 times higher specificity to planar-deposited gold compared with a silicon wafer's native oxide. Following this, representative composite fluorescence images show SYTO 9-stained cells immobilized on patterned gold electrodes with surface areas between 1 and 100 mm² (Fig. 4d). Cell distribution was visibly uniform and spatially defined by the electrode's geometry. Thus, electrode design may potentially be used to guide electrogenetic signal transduction.

To summarize, we confirmed that gold-bound cells could be electroinduced to express sfGFP and LasI (via in situ electrochemical stimulus, Fig. 4e) while maintaining viability and statistically similar peroxide consumption rates to those of planktonic cells (Supplementary Fig. 10). Overall, GBP_3 establishes the surface-assembled, physical connectivity that is important for efficient information flow across the bioelectronic interface.

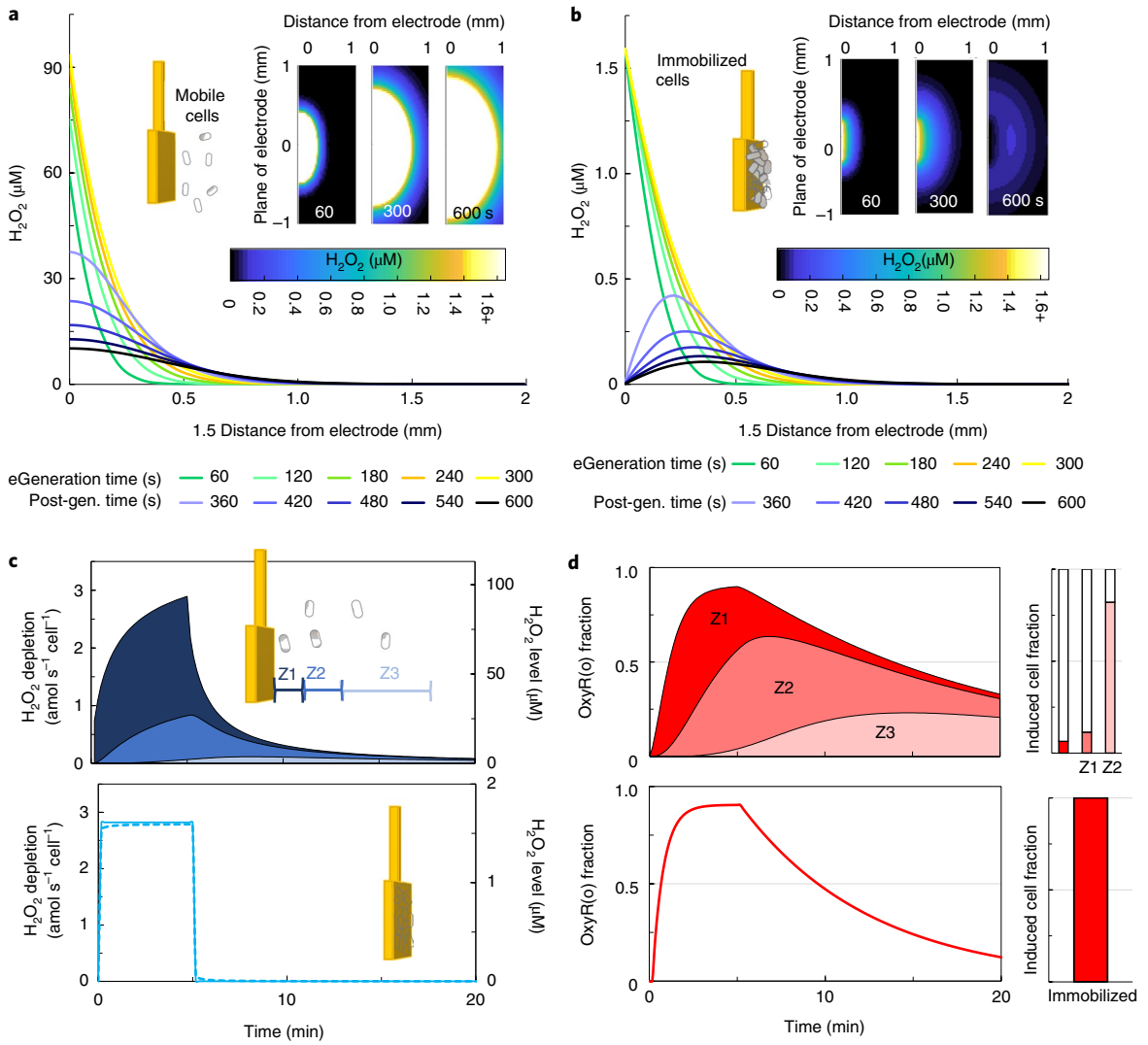

Fig. 3 | Contribution of electrochemical generation and bacterial consumption rates to hydrogen peroxide flux simulated at an electrode. a, Simulation of peroxide flux at a distance from the electrode interface over time, on the basis of the surface-area-dependent rate of charge, the average stoichiometric efficiency of oxygen reduction and the presence of mobile peroxide-consuming cells in the electrode's vicinity. 0–300 s timepoints account for a biased electrode with continuous peroxide generation ('eGeneration'). For 360–600 s timepoints, the electrochemical reaction has been terminated. **b**, Simulation of peroxide flux at an electrode interface, differing from **a** in the positioning of the cells at the electrode interface. **c**, Modelled ranges of peroxide depletion over time, predominantly by cell decomposition, on the basis of peroxide electrogeneration in the presence of mobile cells (tracked across distance intervals from electrode, Z1, Z2 and Z3), and at the electrode interface for immobilized cells. **d**, Projected ranges of OxyR oxidation state over time for cells corresponding to the conditions denoted in **c**. OxyR(o) levels reported as fractions of total intracellular OxyR. Additionally, the population fraction of cells applicable to the OxyR models is reported, on the basis of the cell. For planktonic cells, the peroxide depletion rates in **c** and OxyR(o) fractions in **d** are denoted as a range of values within three zones proximal to the electrode interface: Z1 (0–0.225 mm), Z2 (0.225–0.625 mm) and Z3 (0.625–3.5 mm).

Reflexive verification of signal routing in a bionetwork

We next aimed to (1) propagate the electrogenetic cue across multiple cell populations by redirecting native cell-to-cell communication and (2) enable electrochemical verification of the signal transmission by producing an electrochemically detected redox-active output upon signal exchange. We accomplished this by networking two key cell populations, designated for signal routing and verification respectively (Fig. 5a). First, the electrode-bound cells relay the original electronic signal by actuating an electrogenetic circuit designed to produce LasI-synthesized AHL that is routed via diffusion to the receiving network space. The diffusion space of AHL establishes network boundaries into which planktonic AHL recipients can be connected, for instance, to verify signal strength throughout the network space. We created verifier cells to respond to the routed signal, providing electrochemical feedback, wherein their genetic responses reflected the received signal strength (Supplementary Fig. 11). Specifically, AHL-induced β-gal catalyses production of electrochemically active PAP, which is transduced into an electronic output by its electrochemical oxidation[20,35]. Provided that the electronic output reflects the input status, continuity in information transfer across the bioelectronic interface is thus maintained.

We confirmed that AHL-sensing cells generated an electrochemically detectable output based on β-gal-produced PAP. Differential pulse voltammetry (DPV) of AHL-induced cultures in a PAP-oxidizing voltage range (0.25 to −0.15 V) revealed a faster increase in peak current over time compared with uninduced samples (Fig. 5b). When electrogenetic AHL producers were added

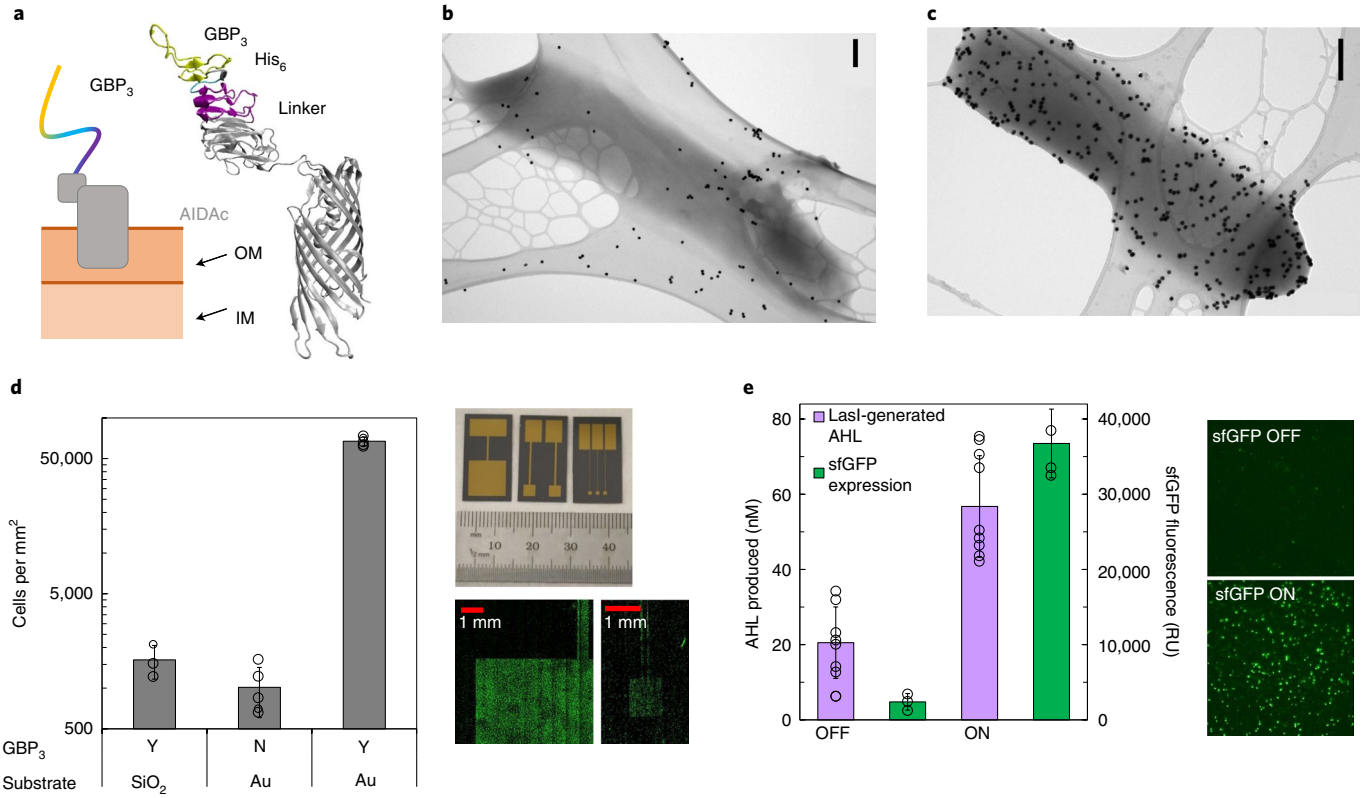

Fig. 4 | Assembly of electrogenetic cells onto gold surfaces via peptide surface display. a, Homology model of AIDA autotransporter structure with an amino-terminally linked fusion of GBP_3 and a hexameric histidine tag. OM, outer membrane; IM, inner membrane. **b**,**c**, Transmission electron micrographs of an *E. coli* cell labelled with 20 nm gold nanoparticles, lacking genes for GBP_3 surface display (**b**) or GBP_3^+ (**c**). Scale bars, 200 nm. **d**, Coverage of *E. coli* cells (−/+ $pGBP_3$) immobilized to either a gold-coated (Au) or uncoated (SiO_2) silicon wafer and stained with SYTO 9. Top inset: photograph of gold electrode chips used in this work alongside a ruler for scale. Bottom inset: composite fluorescent pictures of SYTO 9-stained cells bound to gold electrode chips of 1 cm × 1 cm (left) and 1 mm × 1 mm (right). **e**, Demonstration of electrogenetic activation of gene expression by applying a voltage to electrodes with immobilized cells hosting various reporters (AHL quantified by curve 2 in Supplementary Fig. 1f). RU, relative units. Inset: representative sfGFP fluorescent pictures of gold-electrode-assembled cells that correspond to the OFF and ON conditions in the graph in **e**. Quantification for **d**,**e** is based on three biological replicates per condition and image analysis of technical replicates with s.d. of data reported. Data for individual replicates are shown as open circles.

with electroinduction, the cocultures showed sustained and concomitant production of β-gal and electrochemical readout, both commensurate with charge dose (Fig. 5c). Of note, PAP accumulation over the culture period allows for continuous measurement without sample loss.

Having confirmed that electronic input could be relayed from an electrogenetic router population to recipients, which validated charge input via electrochemical feedback, we assembled the routers onto the electrode to improve signal efficiency. Figure 5d portrays data for this configuration under ON and OFF conditions, where electroinduction occurred in an ON condition (i). Electrode size and representative electrode coverage by router cells were similar between the two conditions (Supplementary Fig. 12). When ON, production of the biological signal, AHL, increased 15-fold (ii), attributed to router activation. Additionally, AHL-induced β-gal expression in verifier cells showed fivefold-enhanced activity in ON samples (iii). Finally, the electronic output of ON cultures was approximately twice as high as the OFF sample output (iv).

With the signal-to-noise ratio (SNR) defined as the ratio of electrochemical readouts between ON and OFF samples, an SNR (Fig. 5e) of two in these experiments was found to be similar among the various system configurations (signal relayed on chip, relayed planktonically and a single-cell-type control, Supplementary Fig. 13). System robustness is demonstrated by noting that the SNR was consistent irrespective of the means of activation (electronic or chemical). The net result demonstrates a complete electronic-to-bio-to-electronic, and thus bidirectional, information exchange with a bacterial community.

Coupling bioelectronic information exchange to actuation

By delocalizing electrogenetics from a discrete surface to a multi-population community through AHL communication, the bioelectronic system exploits native biological signalling processes to accommodate non-electrogenetic cell types. It follows that numerous and distinct populations could be networked in, for example by the inclusion of AHL-responsive cells designated for executive functions as actuators in parallel with electronic feedback from verifier cells. We designed AHL-inducible actuators with identical genetic control to verifiers, so that verifier output also indicates triggered actuator function. In our examples, actuators express and secrete protein products that might influence environments outside the AHL-networked bioelectronics. Protein secretion enables a variety of actuation opportunities based on extracellular biomolecular recognition, interaction or catalytic events. Here specifically, actuator cells cosecrete a natively recognized biotherapeutic peptide, GMCSF, and DsRed as a fluorescent marker (Fig. 6a and Supplementary Fig. 14). GMCSF has therapeutic efficacy for Crohn's disease; its secretion by *E. coli* has been previously accomplished at

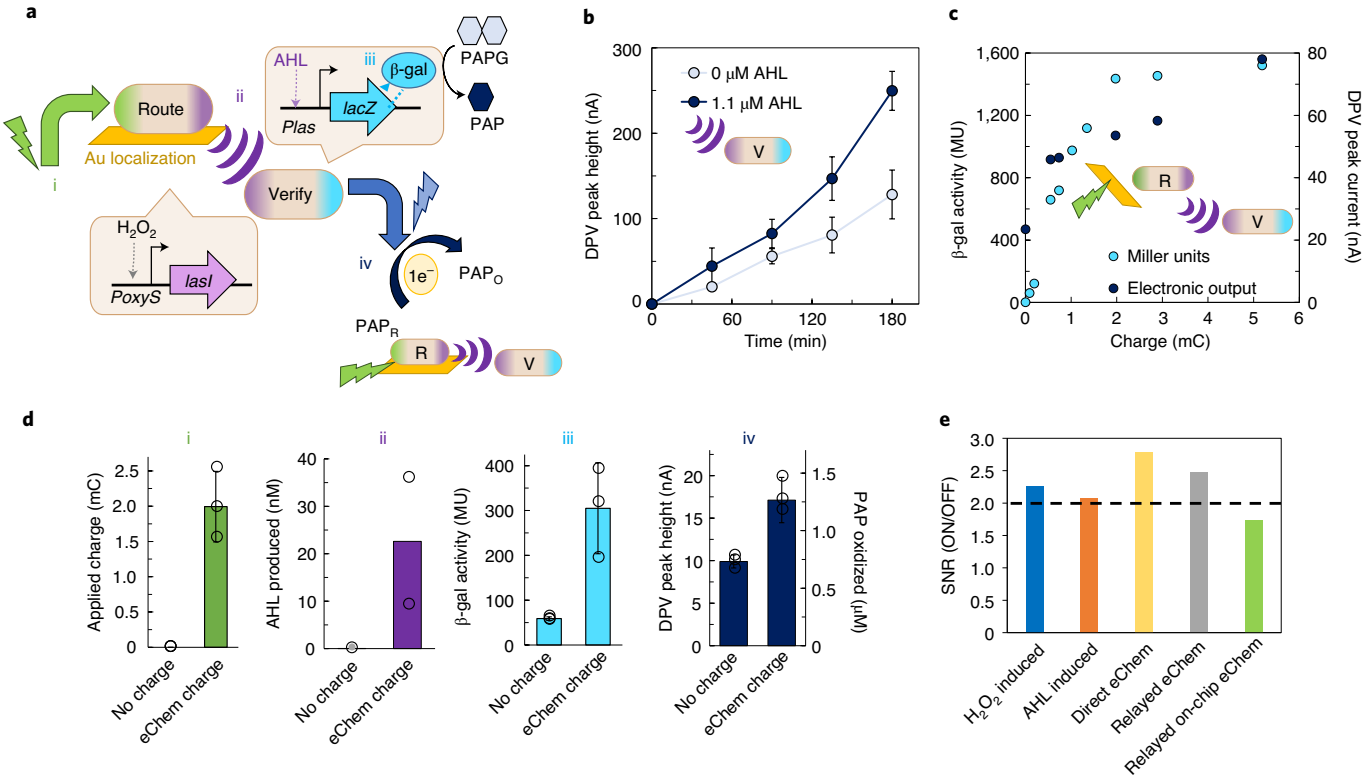

Fig. 5 | Electronic information flow through an engineered two-member community. a, Schematic of information flow from the electrode, through the routing and verification cells with AHL, and back out to the electrode. Redox signals provide transduction between cells and electrodes. **b**, Electronic output, quantified by DPV peak current of PAP oxidation, from verifier cells with or without AHL induction, measured over time. **c**, Verifier cell output, measured both electronically (PAP oxidation current) and with the Miller assay in response to induction with different charges. Routing cells are planktonic. **d**, Indicators of the applied charge (i): AHL production levels (ii); β-gal activity (iii); electronic output of the two-population bioelectronic system described in **a** either with or without applied charge (iv). Means of biological triplicates are shown; error bars indicate s.d. Data for individual replicates are shown as open circles. eChem, electrochemical. **e**, SNRs (ON/OFF) either 1.5 or 3 h after induction. Data are from Supplementary Fig. 13b and Fig. 5b,d.

physiologically relevant levels by coexpression of TolAIII pores.[21] In conjunction, DsRed cosecretion provides optical reporting of the actuators' AHL-responsive function.

We created consortia of varied compositions of router, verifier and actuator cells and probed for their diverse outputs (β-gal, extracellular DsRed and GMCSF) upon AHL signalling. The AHL-driven outputs strongly correlated with the respective population ratios (Fig. 6b), which demonstrates the diversity and resolution of AHL-networked functions. Hence, in addition to electrode size, charge dosage and router genetic circuitry, the population ratio is yet another tunable parameter for multiplexed consortium function.

To illustrate the fully networked bioelectronics system, we established electrochemical connectivity by pairing electrode-bound router cells with the coculture of planktonic verifier and actuator cells. Samples were either maintained in an OFF state or turned ON (−3.4 mC, Fig. 6c(i)). To track the activity of the community, we measured AHL levels (ii), electrochemical output (iii) and product secretion levels (iv) throughout the incubation period. All of the outputs show similar trends for OFF versus ON samples. In OFF samples, AHL, PAP, DsRed and GMCSF levels remained low throughout extended incubations. Conversely, in electronically induced communities, measured outputs increased markedly at 4–10 times higher levels than those in OFF samples. All outputs showed differences between the ON and OFF conditions after 5.5 h and these grew over time. We note that the β-gal substrate supply at 20 h remained sufficient (<10% converted to PAP, Supplementary Fig. 15) to extrapolate this trend beyond the experimental endpoint. This demonstrates bioelectronic input/output successfully directing and reporting distributed biological task execution in a three-member microbial community through an electrochemically triggered and electrochemically read molecular information relay.

This particular consortium grouping is uniquely suited to function as a BioLAN by bioelectronic information exchange between the electronic input/output and AHL-delineated coordination across router, verifier and actuator cells (Fig. 6d). Cell-to-cell communication as exemplified in this BioLAN enables distribution of functions into a collective that is modular and multiplexed by cell type. Further, the consortium members expand the communication repertoire via electronic-transducing redox signals (peroxide, PAP), resulting in a convenient interfacing capability with electronics infrastructure. The electronic information flow can be clearly traced through induction current (Fig. 6e(i)) to the BioLAN output current (Fig. 6e((ii)) to confirm system connectivity as real-time electronic feedback. This, in turn, informs on therapeutic secretion status due to AHL-correlated responses (Fig. 6e(ii)).

Conclusions

This work enables bioelectronic interfacing with a living biological network (BioLAN) by purposing redox molecules to interconvert between electronic and biological input/output to achieve

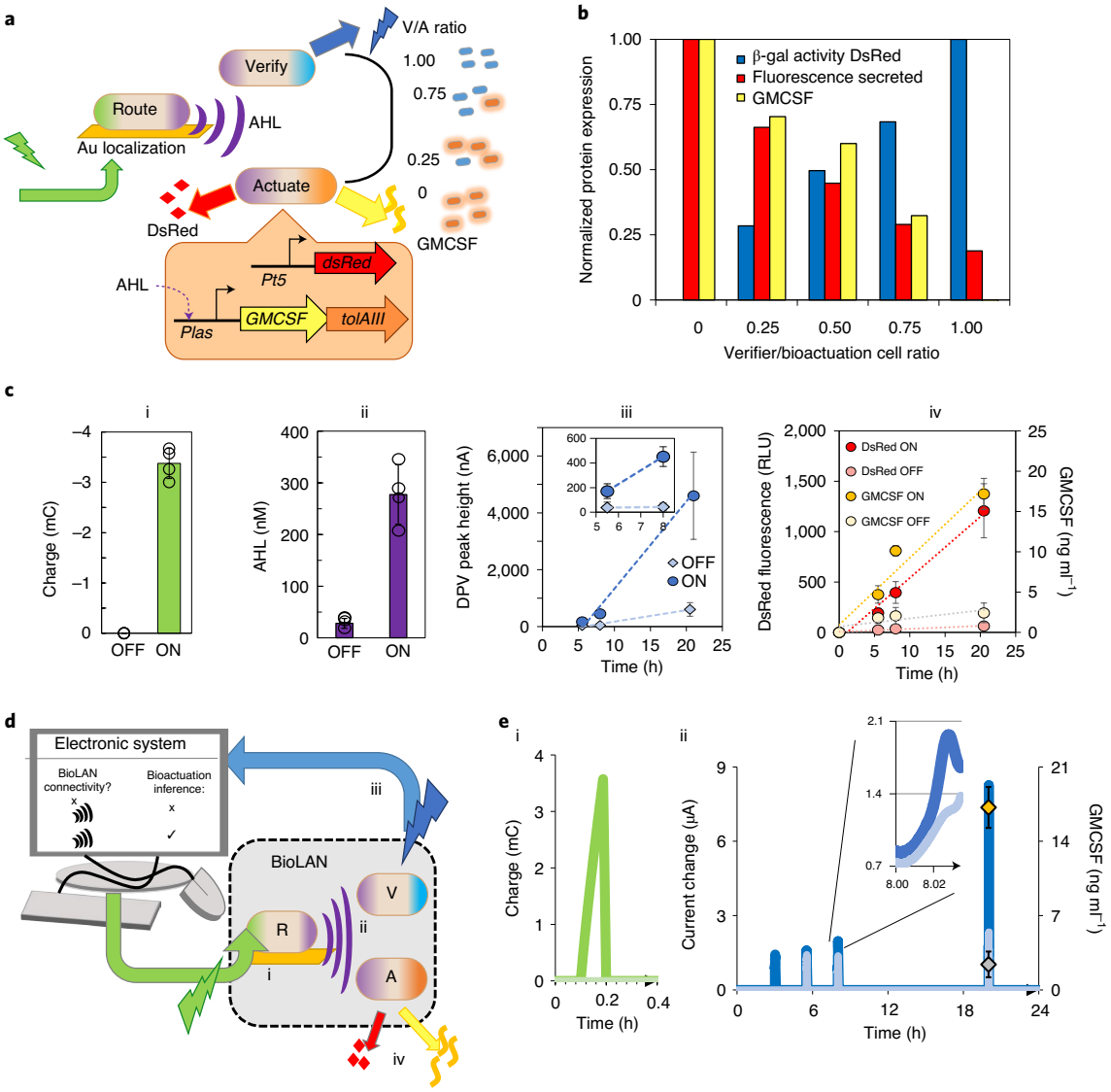

Fig. 6 | BioLAN function. a, Schematic of information flow into the BioLAN, communication between members and BioLAN output. V/A, verifier/actuator. **b**, Normalized protein expression from BioLAN communities in which the indicated ratios of verifier/actuator cells were used. **c**, Measurements of applied charge dose (i), AHL production levels (ii), electronic output from verifier cells (iii) and GMCSF and DsRed production by actuator cells (iv) from BioLAN systems induced electronically with −3.4 mC charge (ON) or kept uninduced (OFF). Individual data for biological quadruplicates are shown (open circles) along with means and s.d. RLU, relative luminescence units. **d**, Schematic showing BioLAN connection to a computer and information flow between them. **e**, Representative traces of real-time measurements of input charge (i) and output current (ii), which precedes the detection of actuator cell production of DsRed and GMCSF (diamonds). Data are representative and correspond to those in **c**.

bidirectional information exchange. Redox signal transduction provides 'wiring' to connect to the synthetic biology, whose electronic proficiency is established by minimal genetic engineering. The engineered cells of the BioLAN have genetically distinct roles of signal routing, verification and actuation, and remain interconnected via internal AHL communication. The BioLAN plugs into the electronics infrastructure to seamlessly transmit information from electronics, through biology, and back out to electronics, and to concurrently drive programmed biological function.

As hydrogen peroxide is a universally recognized redox molecule in biology that can be electrochemically generated, we repurposed native oxidative stress regulation in the BioLAN for electrogenetic expression via the OxyR protein and PoxyS promoter. This newly introduced system functions in aerobic environments and eliminates the need for exogenous mediators. Correlation between modelled peroxide-oxidized OxyR and charge input ensures that electrochemically supplied peroxide is targeted at non-toxic, yet above-threshold, levels for gene expression. Ultimately, voltage-mediated control over the electrogenetic response encodes the BioLAN's ON or OFF status. The electrogenetic cells serve as a router component to distribute the information throughout the BioLAN. This is accomplished by system-specific signal propagation from the electrogenetic cells, which transduce the peroxide input signal into an orthogonal output, AHL. We note that AHL communication is orthogonal to the BioLAN—the microbes require non-native genetically engineered circuitry to recognize AHLs; programmed secretion of alternative molecules could accommodate broader signalling schemes. Native autoinducer AI-2, for example,

would engage natural processes within the BioLAN[36]. Furthermore, multiplexed signalling could independently target designated subpopulations for uniquely timed and carried out tasks.[37]

Electrode localization of router cells improves in situ induction kinetics and avoids diffusion limitations that can lead to heterogeneous responses in suspended biological systems[38], as confirmed by modelling OxyR redox state. Together, we show that the generation of an electrode-localized peroxide flux, its use for bio-electrochemical information transfer and its pairing with the surface-attached cells yields a robust, quasi-solid-state electrogenetic platform. This set-up invites future opportunities for scalable, spatially programmable biological control via three-dimensional, soft, flexible, miniaturized and arrayed electrode formats for wearable, ingestible or other portable systems[39–42]. By combining this hardwired format with 'wireless' signal propagation, one can envision AHL providing a high-fidelity routing capability that extends the network's boundaries to remotely located AHL responders, which could enable direct interfacing with ex situ environments in which a device is deployed.

Given that wireless network components typically return signals to confirm connectivity, the BioLAN includes reflexive feedback. That is, connectivity prompts AHL responders to provide a verification signal directed to the central electronics. Here, verifier cells inform on AHL connectivity via PAP redox output; being mobile, they reflexively signal across the physical boundaries of the network with output signal amplitude as a real-time indicator of connectivity strength. In demonstrations, electronic feedback was measurable for 20+ h after induction, and provided ON/OFF system verification within 3 h. Notably, each component of the BioLAN offers handles for further tuning of signal response times that contribute to the overall system timescale (Supplementary Table 1). The combination of correlative dose–response relationships between charge inputs and outputs with gene expression demonstrated in this work and the added potential for optimizing system response times could feasibly support integrated feedback control for repeated dosing or precise dose adjustments.

Finally, the peripheral BioLAN components should perform electronically programmed functions and thus enable remote bioelectronic actuation. Importantly, because actuator cells homogeneously copopulate the BioLAN with the verifiers and utilize the same AHL-sensitive circuitry, the verifiers' activity implies the status of co-occurring actuation events. We have shown that release of the secreted DsRed and GMCSF payloads accumulated proportionally to the electrochemical readouts over time, validating the electronic output as a proxy of secretion status. Furthermore, actuation offers extended connectivity to external environments based on signal recognition: extracellular fluorescence (DsRed) as optical readout and a secreted biologic for potential in vivo interactions (GMCSF). As potential applications, secreted proteins could enable biorecognition and interactions for healthcare diagnostics and therapy[43], biomolecular self-assembly for biomaterial synthesis[44] or enzymatic catalysis for bioremediation[45].

Signal fidelity across all transduction formats was maintained and was tunable on the basis of population ratio. In this way, the networking of multiple AHL-responsive cell types expands the influence of electrogenetic control, multiplexes outputs and enables the electronic orchestration of complex tasks through signal relay, spatial segregation and division of labour. While one could augment a single cell type to execute multiple functions, such as programming cells to exhibit both actuation and electronic reporting functions, their segmentation into separate populations highlights the potential for distributed networking. Areas such as bioconversion or biosynthesis have interest in such use of consortia[46,47]. Each subpopulation could be individually optimized and the network composition could be autonomously controlled for coordinated, collective function[48,49].

In total, the established bidirectional dialogue represents a hybrid system with electronically programmed and tracked, yet biologically executed, functions. Because redox is both accessed electrochemically and serves as a medium of information exchange, this communication mode presents a reliable platform for plugging in the BioLAN. Moreover, because redox events are inherent within biology, the concepts shown here that couple electroinduction with biological signalling will enable biological connectivity to a variety of electronic devices (for example ingestible capsules, environmental sensors, electronic tattoos and so on)[12,50,51], where readily implemented future developments (Supplementary Table 2) will further augment BioLAN use for these applications. Bioelectronics connectivity featuring synthetic biology suggests a future Internet of Bio-Nano Things[52], yielding applications capable of embedding 'biological intelligence' in ecological settings, wearable interfaces and in vivo environments.

Online content

Any methods, additional references, Nature Research reporting summaries, source data, extended data, supplementary information, acknowledgements, peer review information; details of author contributions and competing interests; and statements of data and code availability are available at https://doi.org/10.1038/s41565-021-00878-4.

Received: 5 March 2020; Accepted: 15 February 2021;
Published online: 29 March 2021

References

1. Gubbi, J., Buyya, R., Marusic, S. & Palaniswami, M. Internet of Things (IoT): a vision, architectural elements, and future directions. *Future Gener. Comput. Syst.* **29**, 1645–1660 (2013).
2. Tian, B. et al. Roadmap on semiconductor–cell biointerfaces. *Phys. Biol.* **15**, 031002 (2018).
3. Atkinson, J. T. et al. Metalloprotein switches that display chemical-dependent electron transfer in cells. *Nat. Chem. Biol.* **15**, 189–195 (2018).
4. Bird, L. J. et al. Engineered living conductive biofilms as functional materials. *MRS Commun.* **9**, 505–517 (2019).
5. Shao, J. et al. Smartphone-controlled optogenetically engineered cells enable semiautomatic glucose homeostasis in diabetic mice. *Sci. Transl. Med.* **9**, eaal2298 (2017).
6. Mimee, M. et al. An ingestible bacterial–electronic system to monitor gastrointestinal health. *Science* **360**, 915–918 (2018).
7. Yang, X. et al. Bioinspired neuron-like electronics. *Nat. Mater.* **18**, 510–517 (2019).
8. Tschirhart, T. et al. Electronic control of gene expression and cell behaviour in *Escherichia coli* through redox signalling. *Nat. Commun.* **8**, 14030 (2017).
9. Bhokisham, N. et al. A redox-based electrogenetic CRISPR system to connect with and control biological information networks. *Nat. Commun.* **11**, 2427 (2020).
10. Sadat Mousavi, P. et al. A multiplexed, electrochemical interface for gene-circuit-based sensors. *Nat. Chem.* **12**, 48–55 (2020).
11. Liu, Y. et al. Connecting biology to electronics: molecular communication via redox modality. *Adv. Healthc. Mater.* **6**, 1700789 (2017).
12. Lee, H. et al. Wearable/disposable sweat-based glucose monitoring device with multistage transdermal drug delivery module. *Sci. Adv.* **3**, e1601314 (2017).
13. Wang, S., Payne, G. F. & Bentley, W. E. in *Gene Expression and Control* (ed. Uchiumi, F.) Ch. 9 (IntechOpen, 2019).
14. Green, J. & Paget, M. S. Bacterial redox sensors. *Nat. Rev. Microbiol.* **2**, 954–966 (2004).
15. Hirose, A., Kouzuma, A. & Watanabe, K. Towards development of electrogenetics using electrochemically active bacteria. *Biotechnol. Adv.* **37**, 107351 (2019).
16. McCarty, N. S. & Ledesma-Amaro, R. Synthetic biology tools to engineer microbial communities for biotechnology. *Trends Biotechnol.* **37**, 181–197 (2019).
17. Lindemann, S. R. et al. Engineering microbial consortia for controllable outputs. *ISME J.* **10**, 2077–2084 (2016).
18. Pomposiello, P. J. & Demple, B. Redox-operated genetic switches: the SoxR and OxyR transcription factors. *Trends Biotechnol.* **19**, 109–114 (2001).
19. Liu, Y. et al. Using a redox modality to connect synthetic biology to electronics: hydrogel-based chemo-electro signal transduction for molecular communication. *Adv. Healthc. Mater.* **6**, 1600908 (2017).

20. VanArsdale, E. et al. Redox-based synthetic biology enables electrochemical detection of the herbicides dicamba and Roundup via rewired *Escherichia coli*. *ACS Sens.* **4**, 1180–1184 (2019).
21. McKay, R. et al. A platform of genetically engineered bacteria as vehicles for localized delivery of therapeutics: toward applications for Crohn's disease. *Bioeng. Transl. Med.* **3**, 209–221 (2018).
22. Zheng, M., Aslund, F. & Storz, G. Activation of the OxyR transcription factor by reversible disulfide bond formation. *Science* **279**, 1718–1721 (1998).
23. Kim, S. O. et al. OxyR: a molecular code for redox-related signaling. *Cell* **109**, 383–396 (2002).
24. Aslund, F., Zheng, M., Beckwith, J. & Storz, G. Regulation of the OxyR transcription factor by hydrogen peroxide and the cellular thiol-disulfide status. *Proc. Natl Acad. Sci. USA* **96**, 6161–6165 (1999).
25. Demple, B. & Halbrook, J. Inducible repair of oxidative DNA damage in *Escherichia coli*. *Nature* **304**, 466–468 (1983).
26. Sultana, S. T. et al. Electrochemical scaffold generates localized, low concentration of hydrogen peroxide that inhibits bacterial pathogens and biofilms. *Sci. Rep.* **5**, 14908 (2015).
27. Rubens, J. R., Selvaggio, G. & Lu, T. K. Synthetic mixed-signal computation in living cells. *Nat. Commun.* **7**, 11658 (2016).
28. Virgile, C. et al. Engineering bacterial motility towards hydrogen-peroxide. *PLoS ONE* **13**, e0196999 (2018).
29. Hornstrom, D., Larsson, G., van Maris, A. J. A. & Gustavsson, M. Molecular optimization of autotransporter-based tyrosinase surface display. *Biochim. Biophys. Acta Biomembr.* **1861**, 486–494 (2019).
30. Terrell, J. L. et al. Nano-guided cell networks as conveyors of molecular communication. *Nat. Commun.* **6**, 8500 (2015).
31. Brown, S. Metal-recognition by repeating polypeptides. *Nat. Biotechnol.* **15**, 269–272 (1997).
32. Tamerler, C. et al. Materials specificity and directed assembly of a gold-binding peptide. *Small* **2**, 1372–1378 (2006).
33. Verde, A. V., Acres, J. M. & Maranas, J. K. Investigating the specificity of peptide adsorption on gold using molecular dynamics simulations. *Biomacromolecules* **10**, 2118–2128 (2009).
34. Medintz, I. L. et al. Quantum-dot/dopamine bioconjugates function as redox coupled assemblies for in vitro and intracellular pH sensing. *Nat. Mater.* **9**, 676–684 (2010).
35. Tschirhart, T. et al. Electrochemical measurement of the beta-galactosidase reporter from live cells: a comparison to the Miller assay. *ACS Synth. Biol.* **5**, 28–35 (2016).
36. DeLisa, M. P., Wu, C. F., Wang, L., Valdes, J. J. & Bentley, W. E. DNA microarray-based identification of genes controlled by autoinducer 2-stimulated quorum sensing in *Escherichia coli*. *J. Bacteriol.* **183**, 5239–5247 (2001).
37. Meyer, A. J., Segall-Shapiro, T. H., Glassey, E., Zhang, J. & Voigt, C. A. *Escherichia coli* "Marionette" strains with 12 highly optimized small-molecule sensors. *Nat. Chem. Biol.* **15**, 196–204 (2019).
38. Servinsky, M. D. et al. Directed assembly of a bacterial quorum. *ISME J.* **10**, 158–169 (2016).
39. Shang, W. et al. Selective assembly and functionalization of miniaturized redox capacitor inside microdevices for microbial toxin and mammalian cell cytotoxicity analyses. *Lab Chip* **18**, 3578–3587 (2018).
40. Pennacchio, F. A., Garma, L. D., Matino, L. & Santoro, F. Bioelectronics goes 3D: new trends in cell–chip interface engineering. *J. Mater. Chem. B* **6**, 7096–7101 (2018).
41. Yuk, H., Lu, B. & Zhao, X. Hydrogel bioelectronics. *Chem. Soc. Rev.* **48**, 1642–1667 (2019).
42. Kang, M. et al. Signal processing approach to probe chemical space for discriminating redox signatures. *Biosens. Bioelectron.* **112**, 127–135 (2018).
43. Hwang, I. Y. et al. Engineered probiotic *Escherichia coli* can eliminate and prevent *Pseudomonas aeruginosa* gut infection in animal models. *Nat. Commun.* **8**, 15028 (2017).
44. Sun, F., Zhang, W.-B., Mahdavi, A., Arnold, F. H. & Tirrell, D. A. Synthesis of bioactive protein hydrogels by genetically encoded SpyTag–SpyCatcher chemistry. *Proc. Natl Acad. Sci. USA* **111**, 11269 (2014).
45. French, K. E., Zhou, Z. & Terry, N. Horizontal 'gene drives' harness indigenous bacteria for bioremediation. *Sci. Rep.* **10**, 15091 (2020).
46. Jiang, Y., Dong, W., Xin, F. & Jiang, M. Designing synthetic microbial consortia for biofuel production. *Trends Biotechnol.* **38**, 828–831 (2020).
47. Jawed, K., Yazdani, S. S. & Koffas, M. A. G. Advances in the development and application of microbial consortia for metabolic engineering. *Metab. Eng. Commun.* **9**, e00095 (2019).
48. Alper, H. S. & Avalos, J. L. Metabolic pathway engineering. *Synth. Syst. Biotechnol.* **3**, 1–2 (2018).
49. Stephens, K., Pozo, M., Tsao, C. Y., Hauk, P. & Bentley, W. E. Bacterial co-culture with cell signaling translator and growth controller modules for autonomously regulated culture composition. *Nat. Commun.* **10**, 4129 (2019).
50. Beardslee, L. A. et al. Ingestible sensors and sensing systems for minimally invasive diagnosis and monitoring: the next frontier in minimally invasive screening. *ACS Sens.* **5**, 891–910 (2020).
51. Windmiller, J. R. et al. Electrochemical sensing based on printable temporary transfer tattoos. *Chem. Commun.* **48**, 6794–6796 (2012).
52. Akyildiz, I. F., Pierobon, M., Balasubramaniam, S. & Koucheryavy, Y. The Internet of Bio-Nano Things. *IEEE Commun. Mag.* **53**, 32–40 (2015).

Methods

Chemicals. PAPG, PAP, *o*-nitrophenyl-β-galactoside (ONPG) and propidium iodide (PI) were from Sigma-Aldrich. PAPG was dissolved in deionized water and PAP and ONPG were dissolved in 0.1 M phosphate buffer. Agar, potassium chloride (KCl), lysogeny broth (LB) (Miller), M9 salts, glucose, glycerol, casamino acids, magnesium sulfate ($MgSO_4$), calcium chloride ($CaCl_2$), 3-(*N*-morpholino) propane sulfonic acid (MOPS) and hydrogen peroxide (H_2O_2, 30%) were from Sigma-Aldrich. AHL was from Cayman Chemicals. Biological fixatives included formaldehyde (Thermo Fisher Scientific) and paraformaldehyde (Electron Microscopy Sciences).

Cell culture and media. Unless otherwise indicated, cells were grown overnight in LB at 37 °C, 250 r.p.m. shaking, inoculated at 1–2% in LB or M9 media, and grown until the indicated cell density (optical density at 600 nm, OD600). M9 media consisted of 1× M9 salts, 0.4% glucose, 0.2% casamino acids, 2 mM $MgSO_4$, 0.1 mM $CaCl_2$ and, optionally, 100 mM MOPS.

Molecular biology and genetic engineering. All enzymes, competent cells and reagents were from New England Biolabs and used according to provided protocols. PCR used Q5 polymerase and the primers in Supplementary Table 6 (gene sequences in Supplementary Table 5). DpnI digestion, polynucleotide kinase phosphorylation, T4 ligations, Gibson assembly and *E. coli* chemical transformation were performed using New England Biolabs product protocols. DNA clean-up, gel extraction and plasmid preparation kits were from Zymo Research and provided protocols were used. Synthetic gene fragments GBP_3 and proD were from Integrated DNA Technologies (IDT). Final plasmid constructs were sequence verified. Constructs included pOxyRS–sfGFP–laa, pOxyRS–LacZ–laa, pOxyRS–LacZ, pOxyRS–LasI–laa, pOxyRS–LasI, pBla–GBP_3, pBla–His_6–AIDA, pBla–linker–AIDA, pAHL–LacZ and pAHL–GMCSF.

Binding of GBP_3^+ cells on chip. Cells were grown overnight in LB medium, diluted in fresh medium and grown until mid-log OD (unless otherwise indicated). Electrodes or precut gold chips were cleaned sequentially in acetone, isopropanol and water solutions, then dried with a nitrogen gas stream, and treated with ozone for 1 h using a PSD series UV ozone system (Novascan Technologies). The immobilization protocol was customized to each strain for at least 40% surface coverage. Small volumes (50–100 µl) of cultures were either applied directly to the surfaces of face-up gold chips to achieve edge-to-edge surface coverage, or alternatively first centrifuged (8,000 r.p.m., 3 min) for fourfold concentration before application. After a 30 min room-temperature static incubation, the cells were washed in PBS face up (each chip placed inside a well of a six-well culture plate) for 15–30 min at 150 r.p.m. Cell-covered electrode chips were incubated in PBS at room temperature until the next steps.

Fluorescent cell staining. To visualize electrode-immobilized bacteria, cells were fluorescently stained using a LIVE/DEAD BacLight bacterial viability kit (Molecular Probes). SYTO 9 and PI were used alone or in combination. In each case, the reagents were diluted between 667- and 1,000-fold in PBS, then applied to the cell-covered surfaces and incubated in the dark for 45 min, undisturbed, to stain immobilized cells. The chips were then rinsed and stored in PBS. Initial characterization of the surface display protein sequence (linker–AIDA, His–AIDA or GBP_3–AIDA) contribution to bacterial immobilization was determined by live-cell imaging, where only the SYTO 9 stain was applied. For subsequent analyses of immobilized cell density, a fixative solution (prepared at 2%) was first applied for 30 min to preserve the samples, followed by a PBS rinse and application of a PI solution before imaging. To quantify viability of cells bound to electrode chips, SYTO 9 and PI were applied in combination, followed by the fixative solution, with PBS rinsing in between steps. In this case, both green and red fluorescence images were captured. To calculate the percentage of dead cells, the total cell area of PI-stained cells in the image was divided by the (PI + SYTO 9)-stained cell area. The fluorescence images were converted to 8 bit, consistently thresholded and the cell areas calculated using ImageJ (NIH). For dead-only staining of planktonic cultures, PI was used at 0.5 mg ml^{-1} in 0.85% NaCl. After 0.5–2 ml of the cell culture (depending on cell density) was pelleted, 50 µl of the PI solution was added, and cells were resuspended and incubated in the dark for 30 min. After a PBS rinse, cell fluorescence was read on a flow cytometer or imaged using a fluorescence microscope.

Fluorescence microscopy. An Olympus BX53 microscope with the 49002-BX3; ET–EGFP/FITC/CY2 470/40X, BS495, 525/50M filter cube was used to visualize sfGFP-producing cells and cells stained with SYTO 9 fluorescent dye. For PI-stained cells the 49008-BX3; ET–MCHERRY/TXRED 560/40X BS585, 630/75M filter cube was used. Additional imaging utilized either an Olympus BX60 for green fluorescence or a ZEISS Axio Observer 7 (Carl Zeiss) with Colibri light-emitting diode illumination and a Filter Set 43 HE Cy3 for red fluorescence. Composite fluorescence images were obtained using a ZEISS LSM700 confocal microscope.

Peroxide electrochemical set-up and generation. For electrochemical peroxide generation a gold-patterned silicon wafer chip (with electrode dimensions 1 cm^2, unless otherwise indicated) was used as a working electrode. A coiled platinum wire (BASi) with surface area larger than that of the working electrode was used as the counter-electrode. An Ag/AgCl (BASi) reference electrode was used. Using sufficient volumes of the indicated solution or media, the electrodes were completely submerged, with the working and reference electrodes in a separate glass vial from the counter-electrode, connected by two salt bridges. The working electrode solution was undisturbed (or, where indicated, stirred with a 7 mm stir bar and a mini magnetic stirrer). The electrodes were connected to a potentiostat (either 700-series CH Instruments or BioLogic VMP3). Chronoamperometry, poised at −0.4 V for the indicated duration, was performed to generate hydrogen peroxide. The endpoint charge was recorded for each run.

Agar salt bridges consisted of 6-inch-long 1.2 mm outer diameter, 0.9 mm inner diameter glass capillary tubes bent into a U shape after brief heating under a Bunsen burner. A 3% agar solution with 1 M KCl was heated and added into the bent capillary tube. Tubes were cooled by immersion in a 3 M KCl solution and stored in 3 M KCl at 4 °C.

Hydrogen peroxide determination. A Pierce quantitative peroxide assay kit (aqueous) (Thermo Fisher Scientific) was used to quantify peroxide according to the manufacturer's instructions. Briefly, the working reagent was prepared by mixing one volume of Reagent A with 100 volumes of Reagent B, with at least 200 µl prepared for each sample to be assayed. Ten volumes of the working reagent were added to one volume of sample (typically 200 µl working reagent to 20 µl sample) in a well of a clear-bottomed 96-well plate. The reaction was mixed and incubated for 15–20 min, after which a SpectraMax M3 plate reader was used to measure the absorbance at 595 nm. Sample peroxide concentration was calculated by comparison with a standard curve (dilutions of 30% peroxide) performed the same day.

Quantification of electrochemical peroxide generation rate. Using experimentally obtained data for peroxide concentration and charge, a characteristic linear relationship was established for both stirring and non-stirring conditions (Supplementary Fig. 5). The efficiency of oxygen reduction to peroxide by the supplied charge was determined by comparing the actual peroxide level with the theoretical yield. The charge was converted to moles of electrons using Faraday's constant (96,485 C mol^{-1}) and accounting for two electrons being required to produce one hydrogen peroxide molecule. The oxygen reduction efficiency was found to be constant at 0.59 regardless of stirring conditions (Supplementary Fig. 5).

Quantification of cell peroxide consumption rates. Cells were grown overnight as above. To quantify consumption of peroxide, T7Express *E. coli* with the pOxyRS–LacZ–laa plasmid was diluted to OD600 values of 0.025, 0.05 and 0.1, each with 100 µM peroxide in 3 ml of LB medium in 15 ml culture tubes in a 37 °C incubator at 250 r.p.m. 20 µl aliquots were assayed at each timepoint, and peroxide levels were compared with a standard curve using the Pierce Quantification peroxide assay kit.

For quantification of peroxide consumption from electrode-immobilized cells, the bacteria were first assembled onto gold-coated wafer chips (150 mm^2) as described in the section Binding of GBP_3^+ cells on chip in the Methods. After rinsing superfluous bacteria from the chips, each was submerged in 2 ml M9 medium supplemented with antibiotics and 100 µM peroxide. The negative control was a sterile gold chip in the solution and the positive control contained suspended cells at an OD600 of 0.025. All samples were incubated statically at 37 °C for 2 h, during which 20 µl aliquots were assayed for peroxide concentration at regular timepoints. At the end of the timecourse, the cell-immobilized chips were fixed with paraformaldehyde, followed by PI staining. Image analysis was used to quantify the exact electrode dimensions on the basis of photographs, and on-chip cell densities on the basis of fluorescence imaging of the chip surfaces. The rate of peroxide accumulation for each sample was determined by normalizing the assay-measured number of peroxide molecules in solution to cell number.

Measurement of growth effects of peroxide. To quantify cell growth in the presence of peroxide, *E. coli* T7Express cells with the pOxyRS–sfGFP–laa and pBla–GBP_3–AIDA plasmids were cultured overnight as described above. The cells were diluted in the M9 medium with antibiotics to an OD600 of 0.025. Either solution-based or electrochemically generated peroxide was added to the cells at different concentrations, as indicated, in triplicate. A Bioscreen C machine (Growth Curves USA) was set up at 37 °C, high shaking, with 400 µl per well, and recorded OD600 measurements every 15 min. The Growth Rates program[53] was used to calculate lag and doubling time.

Colony-forming unit determination. Treated or untreated cells were diluted at least 1,000-fold, and 100 µl of these dilutions were plated on LB + 1.5% agar plates with the appropriate antibiotics. After an overnight incubation at 37 °C, colonies were counted and colony-forming units were calculated.

Flow cytometry. Flow cytometry was used to quantify peroxide-induced sfGFP fluorescence intensity, live/dead cell ratios and quantum dot labelling of cell surfaces. A BD Accuri C6 with an autosampler was used to measure sfGFP and

live/dead cell numbers. Reported values are the mean fluorescence values in the FL-1 channel (green) or FL-3 (red). Quantum dot labelling of cells was determined using a BD Canto II by first establishing a threshold for unlabelled cells using the 530/30 filter and then comparing above-threshold counts between GBP_3^- and GBP_3^+ strains once mixed with quantum dots. All data are supported by at least 20,000 events and consistently gated across samples.

Miller assay. The Miller assay was performed at measurement timepoints according to standard protocols. Briefly, cells were lysed with chloroform and SDS to release β-gal. The substrate ONPG was added and cleaved by β-gal into a yellow molecule, *o*-nitrophenol. The absorbance of sample sets at 600, 550 and 420 nm was quantified using either a SpectraMax M3 or BioTek Synergy plate reader. Absorbance at 600 nm was measured from 250 µl of culture sample before assay preparation and the absorbances at 420 and 550 nm were measured from 200 µl of the sample after assaying for β-gal activity. Miller units were calculated as per the standard protocol.

Electrochemical PAP measurement. PAP was detected electrochemically through cyclic voltammetry, chronoamperometry and DPV. All measurements were performed with a CH Instruments 700-series or VMP3 (BioLogic Science Instruments) using a gold working electrode (2 or 3 mm diameter, CH Instruments), a coiled platinum counter-electrode with working area larger than that of the working electrode (BASi) and an Ag/AgCl reference electrode (BASi). Cyclic voltammograms were run from −0.15 to 0.3 V at a scan rate of 50 mV s^{-1}. The current at the reduction peak was used to measure PAP concentration. DPV was run from −0.16 to 0.36 V, in 2 mV step increments, with a 50 mV amplitude, 0.5 s pulse width and 0.5 s pulse period. The DPV peak height was calculated either automatically or manually for calibration to PAP concentration.

General and coculture electroinduction set-up. The same electrochemical set-up as used for peroxide generation was used for electroinduction, and was placed inside a mini-incubator set at 37 °C. Cells were added to a final OD600 of 0.025 in the working electrode vial, or were preassembled onto the working electrode. M9 medium with the appropriate antibiotics was used. Peroxide was generated via chronoamperometry as indicated above, with voltage application for a specified duration (for example 300 s). For planktonic cells, the entire volume was then pipetted into a culture tube, and placed in a 37 °C shaking incubator at 250 r.p.m., from which samples were removed at indicated time intervals. For electrode-assembled cells, the working electrode was placed in a culture tube with fresh media for shaking incubation at 37 °C and 250 r.p.m. In experiments that electrochemically probed β-gal induction, PAPG was added after electroinduction and before incubation at 5 mg ml^{-1}. For cocultures, the router cells were inoculated to an OD600 of 0.025 in the working electrode solution for planktonic cocultures or preassembled directly on the working electrode, which was submerged in the coculture. In double-culture experiments, the verifier cells were co-inoculated to a final OD600 of 0.1. In triple-culture experiments, verifier and actuator cells were inoculated to a final OD600 of 0.075 and 0.025, respectively (Fig. 6b).

AHL quantification. AHL quantification was performed by bioluminescence assay. AHL reporter cells JLD271 pAL105 were grown overnight in LB at 37 °C and 250 r.p.m. shaking with the appropriate antibiotics. The following day, standard AHL solutions (concentration range) were prepared in LB. The reporter cells were diluted 2,500-fold in LB with the appropriate antibiotics. To each, 90 µl of diluted reporter cells and 10 µl of the standard dilutions were added in a 5 ml culture tube, prepared in duplicate. Experimental conditioned media samples were prepared similarly after sterile filtering and diluting between five- and tenfold to maintain a linear assay range. Culture tubes with reporter cells and conditioned media samples were incubated at 30 °C and 250 r.p.m. shaking for 3 h. Luminescence was measured with a GloMax-Multi Jr (Promega). The AHL concentration of each sample was calculated using the standard curve.

Electrode chip fabrication. Gold electrodes were prepared by cutting gold-coated silicon wafers (Ted Pella) or purchased (Platypus Technologies). The gold coating was 50–100 nm in thickness with a 5 nm sublayer of chromium or titanium. Alternatively, gold electrode arrays were patterned onto silicon wafers. First, metal deposition was performed on standard 4 inch silicon wafers using a Denton thermal evaporator (Denton Vacuum), with metal deposition rates of 2–3 Å s^{-1}. Specifically, a 50 nm chromium adhesion layer was evaporated, followed by 200 nm gold. Next, photolithography utilized direct writing of photoresist via a DWL66fs laser writer (Heidelberg Instruments), guided by a laser exposure map designed in AutoCAD (Autodesk). Photoresist spin-coating and development steps were performed using an EVG120 automated resist processing system (EV Group). The patterned wafer was post-processed by etching, photoresist stripping and cutting individual electrodes with a DAD dicing saw (DISCO).

Protein structure determination. Protein modelling and structural predictions were performed using Phyre2[54]. This approach referenced the 4MEE crystal structure[55] available through the RCSB Protein Data Bank (https://www.rcsb.org/)[56] to generate the homology model of the GBP_3–His–AIDAc protein used in this work.

Protein secretion analysis. The target proteins DsRedExpress2 and GMCSF were analysed. The supernatants of sample aliquots were recovered after centrifugation (6,000 *g*, 2 min) to separate bacteria and subdivided for fluorescence analysis (stored chilled) or immunoassaying (stored frozen). The relative fluorescence intensity of samples was measured using a BioTek Synergy plate reader to determine DsRedExpress2 levels; additional quantification to correlate fluorescence to protein concentration was performed using a Bioanalyzer 2100 (Agilent Technologies). The His-tagged GMCSF peptide was quantified using a His-tag enzyme-linked immunosorbent assay detection kit (GenScript) according to the provided protocol and five- to tenfold dilutions of frozen samples.

Nanoparticle labelling of bacterial surfaces. For quantum dot labelling, CdSe/ZnS core–shell-type quantum dots (Sigma-Aldrich, carboxylic acid functionalized, fluorescence emission wavelength λ_{em} 520 nm) were diluted 100-fold into bacterial cultures (OD600 = 1) resuspended in PBS at a tenfold dilution. After incubating for 1 h at room temperature, the cell cultures were rinsed twice before flow cytometry. For gold nanoparticle labelling, 20 nm gold nanoparticles (Ted Pella, no. 15705-20) were used to label the gold-binding peptide constitutively expressed by *E. coli* cells. Transmission electron microscopy was performed after labelling cells with gold nanoparticles. Cells were diluted in a 2:1 mixture of PBS and water to an OD600 of 0.28. The cells were then mixed with a 1,000-fold excess of gold nanoparticles and incubated for 1 h. The samples were prepared on surface-treated copper grids covered with holey carbon films using a drop-casting method, as described by Dong et al.[57] The samples were viewed with a JEOL 2100 F transmission electron microscope operated at 200 kV.

Model and simulations. The peroxide, promotor and protein expression models were developed using first-order reaction kinetics to describe OxyR kinetics and Hill functions to describe OxyR activation of gene expression. Models were implemented using Microsoft Excel when no spatial resolution was needed. Spatial dynamics were implemented in MATLAB using the built-in PDESolver to solve the diffusion equation. Details are available in Supplementary Methods and Supplementary Table 7.

Implementation of modelled spatial dynamics. To understand the spatial dynamics of peroxide generation and consumption at the electrode with the cells either absent, present on the electrodes or present in solution, the diffusion equation was solved in MATLAB's built-in PDESolver function. The box size was 3.5 mm per side with a 1 mm^2 electrode located in the centre of one face of the box. The geometry was generated using the geometryFromMesh function and 1 µm increments. Peroxide was generated at the electrode for 300 s and then stopped, reflecting a typical pulse increment. The overall simulation was run for 3,600 s. Peroxide consumption either was absent (cell absence), occurred only on the electrode (immobilized cells) or occurred in solution (peroxide pulse into a bulk culture). The details are provided in Supplementary Methods and Supplementary Tables 7 and 8.

Data availability

The datasets that support the findings of this study are available at https://figshare.com/s/30bcc0241826827d12f4. Source data are provided with this paper.

Code availability

The MATLAB code for the models used in this study is available from the corresponding author upon request.

References

53. Hall, B. G., Acar, H., Nandipati, A. & Barlow, M. Growth rates made easy. *Mol. Biol. Evol.* **31**, 232–238 (2014).
54. Kelley, L. A., Mezulis, S., Yates, C. M., Wass, M. N. & Sternberg, M. J. The Phyre2 web portal for protein modeling, prediction and analysis. *Nat. Protoc.* **10**, 845–858 (2015).
55. Gawarzewski, I. et al. Crystal structure of the transport unit of the autotransporter adhesin involved in diffuse adherence from *Escherichia coli*. *J. Struct. Biol.* **187**, 20–29 (2014).
56. Berman, H. M. et al. The Protein Data Bank. *Nucleic Acids Res.* **28**, 235–242 (2000).
57. Dong, H. et al. Living bacteria–nanoparticle hybrids mediated through surface-displayed peptides. *Langmuir* **34**, 5837–5848 (2018).

Acknowledgements

Partial support of this work was provided by DTRA (HDTRA1-19-0021), NSF (DMREF 1435957, ECCS 1807604, CBET 1805274), the National Institutes of Health (R21EB024102) and the Office of Naval Research (N0001417WX01318,

N0001418WX01042). This work was also supported by the Office of the Under Secretary of Defense for Research and Engineering (USD(R&E)) through the Applied Research for Advancement of S&T Priorities (ARAP) Program on Synthetic Biology for Military Environments (SBME).

Author contributions

J.L.T., T.T., Y.L., C.Y.T., H.-C.W., G.V., G.F.P., D.N.S.-C. and W.E.B. were involved with the conception and design of the work. J.L.T., T.T., K.S., R.M. and M.P. were involved with engineering strains used in this work. J.L.T., T.T., J.P.J., K.S. and H.D. were involved with data acquisition and interpretation. J.P.J. and M.M.H. were involved with computational kinetic studies and protein modelling, respectively. J.L.T., T.T., J.P.J., G.F.P., D.N.S.-C. and W.E.B. were involved with writing and documentation of the work.

Competing interests

The authors declare no competing interests.

Additional information

Supplementary information The online version contains supplementary material available at https://doi.org/10.1038/s41565-021-00878-4.

Correspondence and requests for materials should be addressed to W.E.B.

Peer review information *Nature Nanotechnology* thanks Ada Poon and the other, anonymous, reviewer(s) for their contribution to the peer review of this work.

Reprints and permissions information is available at www.nature.com/reprints.